Journal of Materials Chemistry A

PAPER

View Article Online
View Journal | View Issue

Cite this: J. Mater. Chem. A, 2014, 2, 19707

Theoretical insight into highly durable iron phthalocyanine derived non-precious catalysts for oxygen reduction reactions

Min Ho Seo,[a] Drew Higgins,[a] Gaopeng Jiang,[a] Sung Mook Choi,[b] Byungchan Han*[c] and Zhongwei Chen*[a]

N_4-chelate macrocycles comprise the foundation for non-precious metal oxygen reduction reaction (ORR) catalyst research, where the main electrochemical process occurs in polymer electrolyte membrane (PEM) fuel cells. Although iron–nitrogen–carbon (M–N–C) complexes are known to be the most active non-precious ORR catalysts to date, a fundamental understanding of the ORR mechanisms of these materials is still in its nascent stage and needs further investigation. In this work, *ab initio* density functional theory (DFT) calculations have been applied to unveil the underlying principles for the electrocatalytic activity and structural stability of Fe–N_4 chelates exposed to acidic media. Therefore, we compared the electronic structures of ferrous phthalocyanine (Fe-Pc) and an in-house developed Fe-Pc modified with diphenylphenthioether substituent species (Fe-SPc). The results of these DFT simulations directly correlate with the results of the half-cell ORR activity and stability electrochemical testing in 0.1 M $HClO_4$. The results indicate that the relative energetic position of the d_{z^2}-orbital with respect to the Fermi level can induce an Fe redox couple potential shift and modulate the catalytic activity towards the ORR. Furthermore, our combined DFT calculations and empirical observations highlight that the relative position of the d_{z^2}-orbital can be controlled by the incorporation of functional groups, resulting in the ability to tune the ORR activity of these complexes. Structural stability of the materials, as predicted by the DFT-calculated cohesive energies of Fe and FeO, can also be readily tuned by modulating Fe-Pc with the substituent species. This study, coupling rigorous experimental observations with DFT investigations, thereby provides a fundamental insight that can aid in the design of future generations of non-precious ORR catalysts with improved activity and stability.

Received 9th September 2014
Accepted 29th September 2014

DOI: 10.1039/c4ta04690k

www.rsc.org/MaterialsA

1. Introduction

Accurate understanding of oxygen reduction reaction (ORR) mechanisms is vital for improving the efficiency of many devices, including metal-air batteries,[1–5] fuel generation devices[6,7] and fuel cells.[8–14] This issue is highly pertinent to proton exchange membrane (PEM) fuel cells, which are non-polluting electrochemical power generation devices that convert the chemical energy of fuels into electricity, heat and water. Despite the clean and thermodynamically efficient operation of these devices, there are many technical and economic challenges that still prevent their widespread application.[9–11,15–17] The main obstacles include the inherently sluggish ORR kinetics and the low durability of catalysts under the harsh operating conditions.[18–20] Until now, the best and most widely used catalysts are expensive Pt-based materials, owing to their relatively high activity and stability in acidic media[19–22] in comparison to other metal and non-metal based catalysts. The reliance on high-priced Pt catalysts has provided economical motivation to develop various non-precious ORR catalyst materials, including transition metal–N_4 chelate macrocycles, nitrogen-doped carbons, and metal-nitrides, oxides and chalcogenides.[23–27]

Transition metal–nitrogen–carbon (M–N–C) complexes based on iron, first prepared by the heat treatment of Fe–N_4 chelate macrocycles, or more recently, relatively inexpensive inorganic and organic precursors,[26–32] have emerged as the most promising non-precious catalysts. It is a well-established fact that heat treatment at temperatures ranging from *ca.* 700 to 1000 °C is important for imparting high catalyst activity and stability. However, significant structural reconfiguration and the heterogeneous complexity of the M–N–C materials resulting

[a]*Department of Chemical Engineering, Waterloo Institute for Nanotechnology, Waterloo Institute of Sustainable Energy, University of Waterloo, 200 University Ave. W, Waterloo, ON, N2L 3G1, Canada. E-mail: zhwchen@uwaterloo.ca; Fax: +1-519-746-4347; Tel: +1-519-888-4567 ext. 38664*

[b]*Surface Technology Division, Korea Institute of Materials Science (KIMS), Changwon 641-010, South Korea*

[c]*Department of Energy Systems Engineering, School of Materials Science and Engineering, Daegu Gyeongbuk Institute of Science and Technology (DGIST), Daegu, 711-873, South Korea. E-mail: hanbc@dgist.ac.kr; Fax: +82-53-785-6409; Tel: +82-53-785-6412*

from the heat treatment have led the majority of studies to rely on trial-and-error-based approaches. These investigations involve the empirical optimization of various thermodynamic and kinetic variables, and they are performed by systematically varying the catalyst synthesis procedures (*i.e.* precursor types and concentrations, mixing/blending strategies, heat-treatment temperatures and treatment durations, post-treatment procedures, *etc.*). In addition, a poor understanding of the active sites in M–N–C catalysts has further made the fundamental mechanisms underlying the ORR activity and stability immensely challenging to elucidate. Without this knowledge, it is impossible to apply rational design strategies to prepare non-precious ORR catalysts with improved activity and stability in PEM fuel cells.

Previously, we reported a new iron phthalocyanine (Fe-Pc)-based material functionalized with four diphenylphenthioether substituent species (Fe-SPc) as a non-precious ORR catalyst and investigated the half-cell electrochemical properties in 0.1 M $HClO_4$.[33] Fe-SPc was prepared *in lieu* of a pyrolysis process, enabling us to adequately control the atomic structure and surface properties of the Fe-SPc materials. A significantly improved electrochemical stability of Fe-SPc was observed in comparison to the Fe-Pc catalyst. This could be attributed to the incorporation of thioether substituent groups that were speculated to provide electron-donating capabilities to the metal-ion center. Conclusively explaining the electrochemical performance variations between Fe-Pc and Fe-SPc and understanding the electronic structure–property relationships of this class of materials will provide valuable fundamental insights that could guide future catalyst design endeavors.

In order to fundamentally elucidate the structural properties and to explain the empirical results with a fundamental mechanistic understanding of the underlying catalysis for a variety of different materials and reactions, *ab initio* computational methods using density functional theory (DFT) have emerged as an extremely useful tool.[34–37] For example, *ab initio* computational studies have been used to confirm Sabatier's principle, where a good electrocatalyst should moderate the chemical interactions with the reaction intermediates.[34–37] This has led to the proposition that a simple electronic structure parameter, the d-band center, could successfully dictate the ORR kinetics occurring on a wide array of materials.[38–41] According to this principle, the N4-chelate macrocycles should also provide finite chemisorption energies between the oxygen intermediates and the ORR active surface sites, and a certain value exists that can maximize the ORR turnover frequencies.

It is known that the electronic structure of a metal ion can be modified by the surrounding π-conjugated ligand topologies, thereby causing a change in its redox potential.[34,42,43] This indicates that variations in the electronic properties of the overall macrocycle structures are governed by contributions from both the metal-ion center as well as the surrounding ligand structure. As such, it is necessary to prepare well-defined model systems and to develop accurate molecular orbital analysis to acquire a fundamental understanding of the ORR catalytic activity. In the present work, we utilize first principles DFT calculations to understand the particular mechanisms governing the catalytic activity and structural stability of Fe-SPc and Fe-Pc materials from the perspective of macrocycle electronic structure. Empirical electrochemical measurements published previously[33] were used in combination with molecular orbital analysis to identify the key fundamental factors controlling the ORR activity and long-term stability, most importantly the electron transfer mechanisms occurring at the molecular scale.

2. Computational design and experimental procedures

Computational details

Density functional theory (DFT)[44,45] calculations implemented in the Vienna *ab initio* simulation package (VASP)[46] program were utilized for the present study. Exchange-correlation energies of electrons are described by the Perdew–Burke–Ernzerhof (PBE) functional[47] for generalized gradient approximation (GGA).[48] Core electrons were replaced by the projector augmented wave (PAW) pseudo-potentials,[49,50] and Kohn-Sham wave functions of valence electrons were expanded by a plane wave basis set with a cutoff energy of 520 eV. The designed Fe-Pc and Fe-SPc are located at the center of the vacuum cube box, having lengths of 40 Å for the x, y and z directions. The atoms and cell parameters of each structure were fully relaxed, and spin polarized calculations were subsequently performed. A Gamma point mesh of $1 \times 1 \times 1$ was used to calculate the density of states (DOS) and for finding the thermodynamically stable Fe-SPc and Fe-Pc structures with a Gaussian-smearing width of 0.2 eV.[51,52]

Synthesis of ferrous 2,9,16,23-tetra(2′,6′-diphenylphenthio ether) phthalocyanine (Fe-SPc)

Fe-SPc was prepared according to the method reported in our previous study.[33] In brief, and depicted schematically in Fig. 1. 4-Nitrophthalonitrile and $Fe(OAc)_2$ were dissolved in 100 ml of quinolone and stirred at 483 K under N_2 protection. After 24 hours, methanol was added to precipitate the materials, and a green powder consisting of ferrous 2,9,16,23-tetranitro phthalocyanine (Fe-(nitro)Pc) was obtained by purification with column chromatography on a silica gel, with pyridine as the eluent. The 2,6-diphenylthiophenol, Cs_2CO_3, *N*-methylpyrrolidone (NMP), and toluene were stirred at 418 K under N_2 atmosphere until the water and toluene evaporated, and the

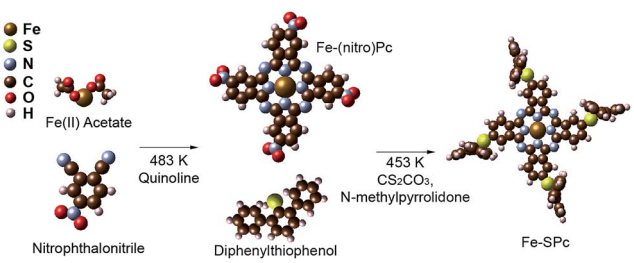

Fig. 1 Schematic illustration of the synthesis of Fe-SPc.

mixture was cooled down subsequently. The prepared Fe-(nitro) Pc was then added into the reaction mixture under N_2 protection and heated at 453 K, with constant stirring for 12 h. After cooling, the mixture was poured into methanol to precipitate the resulting green powder, which was then purified by column chromatography on silica gel with dichloromethane.

Electrode preparation and electrochemical measurements

The electrode preparation and electrochemical analysis carried out previously are summarized in this section.[33] Electrochemical measurements were performed *via* cyclic voltammetry (CV) using a bipotentiostat (PINE research instrumentation). The half-cell system consisted of a pre-treated glassy carbon working electrode (0.196 cm^2), a platinum wire counter electrode and a reference electrode (Reversible Hydrogen Electrode, Hydroflex™, RHE). The Fe-SPc was refluxed for 2 h on KJ300, which was sonicated in 1,2-dichloroethane. The Fe-SPc/KJ300 was then collected after the solvent was distilled off. 20 mg of Fe-SPc was dissolved in 5 mL of 1,2-dichloroethane at the same time. Catalyst inks were prepared as follows: 2 mg catalyst samples were suspended in 1 mL of ethanol and a Nafion® ionomer solution (5 wt%) and sonicated. Subsequently, 60 μL of the catalyst solution was pipeted out and transferred to the working electrode. N_2 or O_2 gas was purged into the electrolyte for at least 30 min before performing electrochemical measurements. The ORR polarization curves for the RDE were obtained in an O_2-saturated 0.1 M $HClO_4$ solution at room temperature. A positive sweep was performed at a scan rate of 10 mV s^{-1} and at the electrode rotation rates of 400, 900, 1600 and 2500 rpm.

3. Results and discussion

To understand the mechanistic origin of ORR activity and structural stability of Fe-SPc in acidic conditions, four possible positional isomers (*e.g.* C_s, C_{2v}, D_{2h} and C_{4h} symmetry) were designed by replacing the H atoms on each of the four external heterocycles in Fe-Pc with diphenylthiophenol substituent groups. The C_{4h} structure showed the most stable structure, which is consistent with our previous reports.[33] Fig. 2a and b show the DFT optimized Fe-Pc and Fe-SPc structures, respectively. The structure of Fe-Pc was optimized as a nearly planar macrocycle structure, whereas Fe-SPc appeared to undergo structural distortion owing to the diphenyl thiophenol groups. The bond lengths between the central Fe atom and surrounding N atoms were denoted as N1, N2, N3 and N4 in Fig. 2 and were calculated to be *ca.* 1.93–1.94 Å in Fe-Pc as summarized in Table 1. This was also consistent with previous reports.[53] It has been proposed that the changes in the molecular geometry, particularly the Fe–N bonding lengths, arise due to the modulated electronic properties of the metal-center, induced by the effect the diphenyl thiophenol groups on the surrounding ligand structures in Fe-SPc.[24,33,44,45] We verified this speculation by calculating the atomic partial charges on Fe-Pc and Fe-SPc and by relating the structural change to the nature of the Fe metal-center. We believe that the central Fe-ion may have significant

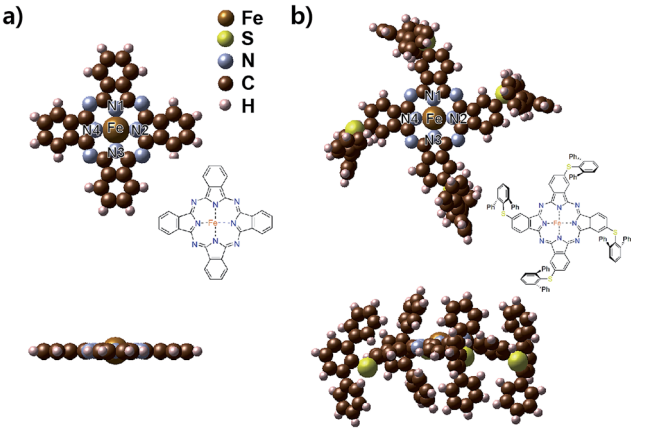

Fig. 2 Top and side views of the model structures for (a) Fe-Pc and (b) Fe-SPc.

orbital hybridizations with the surrounding N atoms, thereby affecting the catalytic performance. Fig. 3a and b display the differences in the charge density, which are defined by eqn (1) given below,

$$\rho = \rho_{\text{Fe-(S)Pc}} - \rho_{\text{C}} - \rho_{\text{N}} - \rho_{\text{H}} - \rho_{\text{Fe}}(-\rho_{\text{S}}) \quad (1)$$

The yellow and blue areas in Fig. 3 indicate the electronic charge accumulation and depletion, respectively. Both Fe-Pc and Fe-SPc show that the electronic charge distribution is symmetric, and that the charges are accumulated around the nitrogen (N) atoms owing to its high electronegativity (3.04) on the Pauling scale.[54] The central Fe-ion in Fe-Pc demonstrates a depletion of charge, whereas the addition of electron-donating diphenyl thiophenol functional groups on Fe-SPc leads to charge accumulation. The projected density of states (PDOS) of the valence Fe electrons are provided in Fig. 4, demonstrating that the electronic structure of Fe-SPc changes significantly with respect to Fe-Pc. The DOS of Fe in Fe-Pc and Fe-SPc displayed in Fig. 4a and b, respectively, demonstrate bonding-antibonding splitting, which provides indication of the strong chemical bonds between the metal and non-metal atoms.[38,55,56] The octahedral environment gives rise to doubly and triply degenerated e_g and t_{2g} sets, which consist of the axial orbitals of $d_{x^2-y^2}$ and d_{z^2}, and the interaxial of d_{xy}, d_{xz}, and d_{yz} orbitals.[34,43,57,58] Fig. 4 demonstrates occupied and unoccupied molecular orbitals for the ground states of the Fe-Pc and Fe-SPc molecules. For the Fe-Pc and Fe-SPc with a local octahedral symmetry (or square planar symmetry, C_{4h}) coordination of the Fe center, the uppermost band is made up of $d_{x^2-y^2}$ levels, an observation consistent with previous reports.[34,43,57–59] In the PDOS for the 3d electrons of Fe in Fe-Pc (Fig. 4a), the electrons of Fe-t_{2g}-like bands (*e.g.*, d_{xy}, d_{xz}, and d_{yz}) in the up-spin state are almost fully occupied, whereas those in a down-spin state are half-filled near the Fermi level. In contrast, adding a diphenyl thiophenol functional group on Fe-Pc shifts the Fermi energy to a more positive value, and the electronic t_{2g}-like orbital near the Fermi level is fully filled for Fe-SPc. This can be attributed to the

Table 1 Bond lengths between the Fe and N atoms, O and O_2 adsorption energies, and the cohesive energies of Fe and FeO in the investigated Fe-Pc and Fe-SPc structures

	Fe–N1 (Å)	Fe–N2 (Å)	Fe–N3 (Å)	Fe–N4 (Å)	$E_{ads\text{-}O}$ (eV)	$E_{ads\text{-}O_2}$ (eV)	$E_{coh\text{-}Fe}$ (eV)	$E_{coh\text{-}FeO}$ (eV)
Fe-Pc	1.934	1.934	1.934	1.938	−4.02	−0.92	9.80	10.15
Fe-SPc	1.938	1.941	1.925	1.924	−4.37	−0.98	9.53	10.22

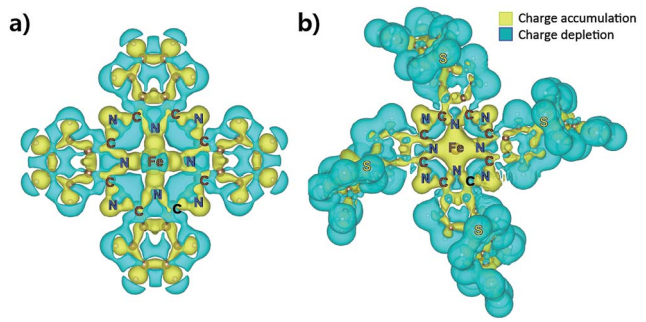

Fig. 3 Charge density changes of Fe-Pc and Fe-SPc.

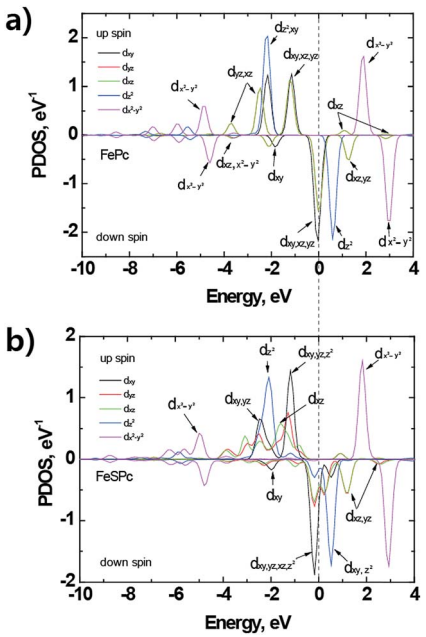

Fig. 4 PDOS for (a) Fe-Pc and (b) Fe-SPc, calculated with the d_{xy}, d_{xz}, d_{yz}, $d_{x^2-y^2}$ and d_{z^2} orbitals using the DFT methods. All the densities of states are shifted such that the Fermi energy is numerically equal to zero.

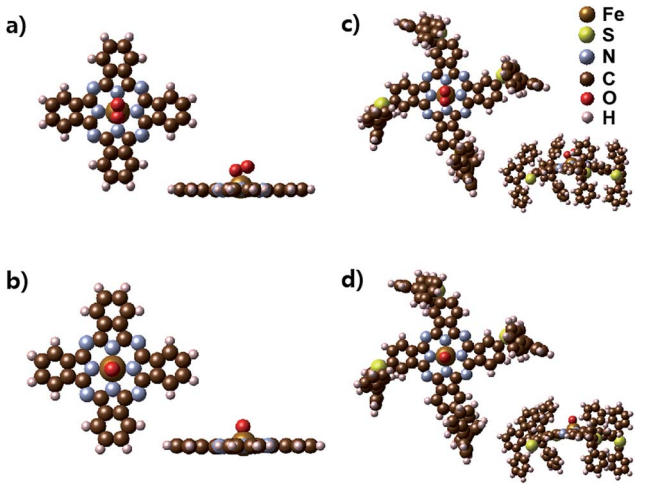

Fig. 5 Top and side views of the model structures for the O_2- and O-adsorbed (a and b) Fe-Pc and (c and d) Fe-SPc.

additional electrons provided by the ring ligands, as demonstrated in Fig. 3.

To understand the ORR activity mechanism from molecular orbital analysis, we designed model systems including either O_2 or O adsorbed on Fe-Pc and Fe-SPc, as shown in Fig. 5. From the optimized structures, the bonding lengths between Fe and the nearest neighbored O atom of O_2, which were directly associated with the adsorption energy of O_2 on the Fe present in the macrocycle complexes, were evaluated to be 1.813 Å and 1.812 Å for Fe-Pc and Fe-SPc, respectively. Fig. 6a and b illustrate that the $d_{x^2-y^2}$ orbital in the projected-density of states (PDOS) does not directly link with the O_2 adsorption on both Fe-Pc and Fe-SPc, showing that the peaks for the $d_{x^2-y^2}$ orbital are in fact formed without the effect of split-off bands, thereby indicating strong chemisorption. However, Fig. 6c and d show that the electronic d_{z^2} orbital is spilt into bonding and antibonding states before and after the adsorption of O_2, suggesting that the d_{z^2} orbital in the PDOS is more or less a dominant factor influencing the ORR activity. This in turn highlights that the d_{z^2} orbital is closely linked with the redox potential of the Fe-ion, a value that has been well established to govern the onset potential for ORR on these macrocycle materials.[34,60–62] The triangles in Fig. 6c and d demonstrate that the level of the d_{z^2} orbitals in the up-spin state and under the Fermi level in Fe-SPc is shifted upwards in comparison to the Fe-Pc shift from −2.158 eV to −2.085 eV.

To truly identify the relationship between the d_{z^2} orbital and the ORR activity, the Fe-SPc and Fe-Pc supported on KJ300 were subjected to rotating disk electrode (RDE) voltammetry, as shown in our previous work.[33] The ORR is a multi-electron transfer reaction with two primary pathways.[63–65] The first step involves the transfer of two electrons to produce hydrogen peroxide,[63–65] H_2O_2, and the second is the direct four-electron pathway that produces water, H_2O, described by the following set of reactions (2 and 3):[63,65]

$$O_2 + 2H_2 + 2e^- \rightarrow H_2O_2 \quad (2)$$

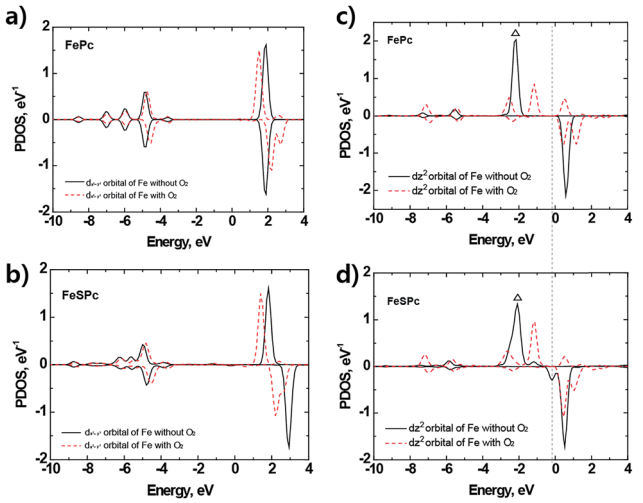

Fig. 6 PDOS of (a and b) $d_{x^2-y^2}$ and (c and d) d_{z^2} orbitals in (a) Fe-Pc and in (b) Fe-SPc before/after the adsorption of O_2, as calculated using the DFT methods. All the densities of states are shifted, so that the Fermi energy is numerically equal to zero.

$$O_2 + 4H^+ + 4e^- \rightarrow 2H_2O \quad (3)$$

The ORR polarization curves of the catalysts were obtained at rotation rates varying from 400 to 2500 rpm in an O_2-saturated 0.1 M $HClO_4$ electrolyte. After removing the background currents to eliminate capacitive contributions, the number of electrons transferred for the reduction of O_2 on both Fe-Pc and Fe-SPc was calculated to be *ca.* 4, using the Koutecky–Levich eqn (4) (ref. 66 and 67) mentioned below:

$$i_d = 0.62 n_e F S D_{O_2}^{2/3} \nu^{-1/6} c_0 \omega^{1/2} = B\omega^{1/2} \quad (4)$$

here, i_d is the disk current density, n_e is the number of electrons transferred per molecule of O_2, F is Faraday's constant, S is the geometric surface area of the electrode, D_{O_2} is the diffusion coefficient of the dissolved O_2 in the electrolyte, ν is the kinematic viscosity of the electrolyte, ω is the electrode rotation rate in radian s^{-1}, c_0 is the concentration of the dissolved O_2 in the electrolyte and B is the Levich constant. In Fig. 7a, as previously reported,[33] the polarization curves were obtained in O_2-saturated 0.1 M $HClO_4$ at 298 K using a potential scan rate of 10 mV s^{-1} from 0 to 1.0 V *vs.* RHE and at the rotation speed of 400 rpm. Here, Fe-Pc/KJ300 demonstrates an increased on-set potential and a half-wave potential (0.62 V *vs.* RHE), which is 20 mV higher than that of Fe-SPc/KJ300 (0.60 V *vs.* RHE), indicating better ORR performance without the addition of the diphenyl thiophenol substituent groups.

The first electron transfer to the adsorbed O_2 to form the superoxide species is generally considered the factor that governs the onset potential for ORR.[61,68,69] The mechanism can be expressed by eqn (5) and (6):

$$O_2 \rightleftharpoons O_2^* \quad (5)$$

$$O_2^* + e^- \rightleftharpoons O_2^- \quad (6)$$

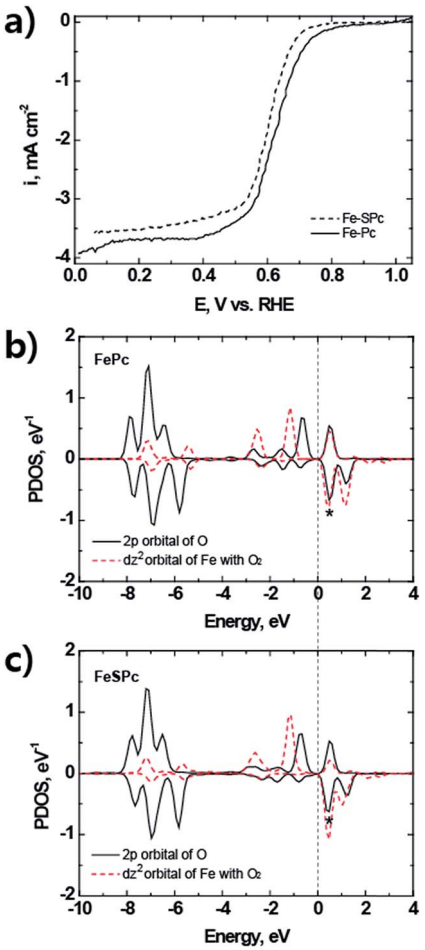

Fig. 7 (a) Polarization curves on Fe-Pc/KJ300 (straight line) and Fe-SPc/KJ300 (dashed line) for the ORR in the O_2-saturated 0.1 M $HClO_4$. PDOS of O_2 2p and Fe d_{z^2} orbitals in O_2 adsorbed (b) FePc and (c) Fe-SPc calculated using the DFT methods. All the densities of states are shifted so that the Fermi energy is numerically equal to zero. The experimental data for (a) is reproduced from ref. 23, Copyright 2010, with permission of The American Chemical Society.

Here, O_2^* is the adsorption of O_2 onto catalyst surface. The energy difference (ΔO2p) between the Fermi level and the peak positions of the unoccupied O2p orbital, denoted by an asterisk in the PDOS for the adsorbed O_2 (Fig. 7b and c), could provide insight into the first electron transfer reaction (5), wherein the smaller ΔO2p values indicate an easier electron transfer. The energy level of the O2p orbital in the antibonding states of O_2 with down spin states are 0.477 eV and 0.481 eV for Fe-Pc and Fe-SPc, respectively. Therefore, the higher onset potential of Fe-Pc in Fig. 7a could be interpreted from the computational results, which indicate that the ΔO2p value of Fe-Pc is smaller than that of Fe-SPc, leading to a relatively easier electron transfer to the O atom, thereby improving the ORR kinetics. From these observations, it can be inferred that the lower ORR onset potential of Fe-SPc is attributed to the electronic structure changes of the central Fe atom, induced by adding the electronic donating substituents, which result into an upward shift of the e_g (d_{z^2}) orbital and limit the electron transferability to the adsorbed O_2 molecules.

Using the calculated thermodynamics of different intermediates, we make direct comparisons to voltammetric and rotating ring disk electrode experiments, to evaluate the electrochemical activity of the Fe-Pc and Fe-SPc surface for the ORR. With the DOS studies, thermodynamic free energy diagrams were calculated to define a rate-determine step of the ORR on the Fe-Pc and Fe-SPc surfaces. Four electron reaction pathways were considered, as shown in eqn (7)–(10):

$$O_2(g) + 4H^+ + 4e^- \rightleftharpoons OOH^* + 3H^+ + 3e^- \quad (7)$$

$$OOH^* + 3H^+ + 3e^- \rightleftharpoons O^* + H_2O(l) + 2H^+ + 2e^- \quad (8)$$

$$O^* + H_2O(l) + 2H^+ + 2e^- \rightleftharpoons [OH]^* + H_2O(l) + H^+ + e^- \quad (9)$$

$$[OH]^* + H_2O(l) + H^+ + e^- \rightleftharpoons 2H_2O \quad (10)$$

The details regarding the ORR free energy diagram calculations are well-described in the previously published reports.[70–73] Briefly, the free energy of any ORR intermediate with respect to liquid H_2O (ΔG) was calculated using eqn (11):

$$\Delta G = \Delta E + \Delta ZPE - T\Delta S \quad (11)$$

here, ΔE, ΔZPE and ΔS denote the DFT-calculated ground state energy, zero point energy, and entropy corrections, respectively. The ΔZPE for intermediates were adopted from Nørskov *et al.*,[70] which used ΔS at $T = 298$ K, as presented by a thermodynamic table.[70,74] The effect of the potential was evaluated at pH = 0 by shifting the electronic chemical potential according to Nernst's law. Fig. 8 demonstrates the free energy change of each ORR step for the ideal, Fe-Pc and Fe-SPc at zero electrode potential (Φ = 0V *vs.* RHE), and at the potential for which all steps become energetically negative. At the equilibrium potential ($U = 1.23$V), the O* formation is energetically negative (exothermic) and all other step are positive (endothermic) for both Fe-Pc as well as Fe-SPc. By applying the overpotential, all the steps become negative for the ORR at 0.67 V and 0.59 V *vs.* the RHE on the Fe-Pc and Fe-SPc, respectively. The calculated thermodynamic free energy diagram predicts that the Fe-SPc activity is lower than that of the Fe-Pc activity, consistent with the RDE experimental results. With even a slightly lower overpotential than the potential at which every reaction step is energetically negative (*i.e.*, 0.67 and 0.59 V *vs.* RHE for Fe-Pc and Fe-SPc), the reduction step of O* to OH* will become energetically positive, revealing that the O*/OH* exchange is the rate-determining step for the ORR.

To investigate the impact of adsorption strength on the ORR activity, the adsorption energy (E_{adss}) of the O or O_2 molecules on these macrocycle complexes were calculated using eqn (12):

$$E_{ads} = E_{O_{(2)}Fe\text{-}(S)Pc} - E_{Fe\text{-}(S)Pc} - E_{O_{(2)},g} \quad (12)$$

here, $E_{O_{(2)}Fe\text{-}(S)Pc}$, is the total energy of O or O_2-adsorbed Fe-Pc and Fe-SPc, $E_{Fe\text{-}(S)Pc}$ is the total energy of Fe-Pc and Fe-SPc, and $E_{O_{(2)},g}$ is the total energy of O_2 (or O) in vacuum. The DFT O_2 and O adsorption energies of Fe-SPc were calculated to be −0.98 eV and −4.37 eV, respectively, which are higher than −0.92 eV and −4.02 eV relative to Fe-Pc. The Fe–O bonding lengths of 1.644 Å and 1.642 Å and the Fe–O_2 bonding lengths of 1.813 Å and 1.812 Å were determined for Fe-Pc and Fe-SPc, respectively. These results demonstrate that larger adsorption energies could result into shorter bonding distances. Therefore, the relatively upward shift of the d_{z^2} orbital of the Fe atoms provides stronger bonding of oxygen intermediates onto Fe-SPc, as indicated by our computational analysis. It can be interpreted that this enhanced adsorption strength with oxygen intermediates on Fe-

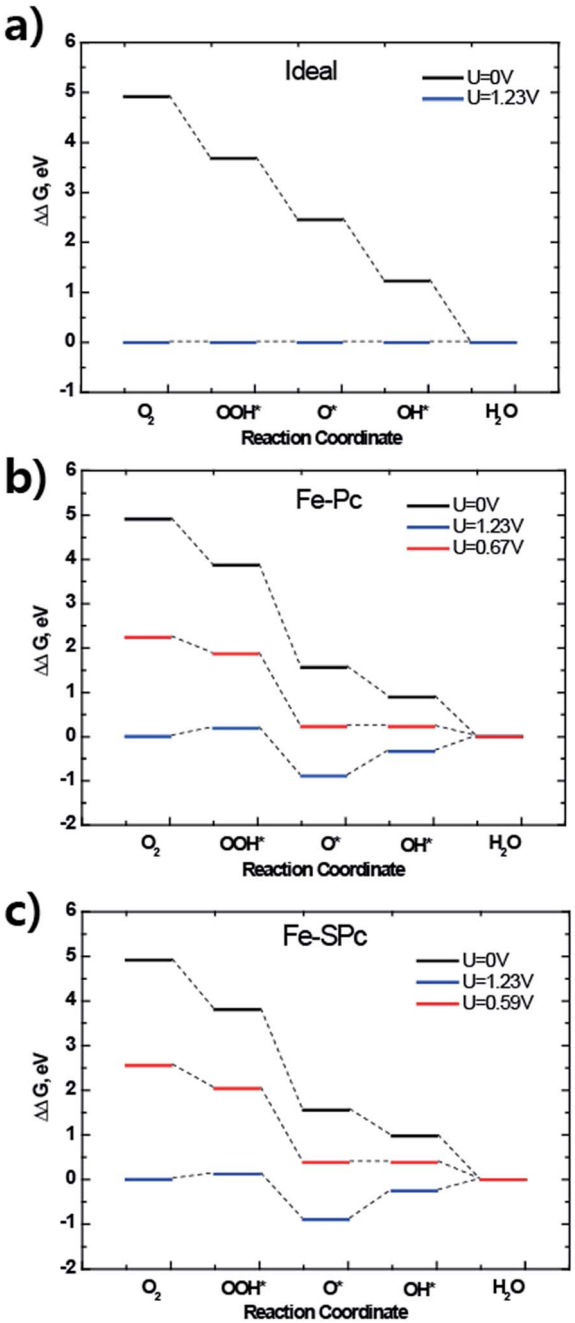

Fig. 8 Standard free energy diagram of (a) ideal, (b) Fe-Pc and (c) Fe-SPc for the ORR at zero potential ($U = 0$), equilibrium potential for ORR (U = 1.23 V) and at the potential for which all the steps become energetically negative at pH = 0 and at $T = 298$ K.

SPc is too strong to obtain a high activity for the ORR. Accordingly, a downshift in the energy level of the d_{z^2} orbital away from the Fermi level leads to a shift in the Fe ion's redox potential, and by extension, results into smaller ΔO2p values and higher ORR activity potentials. In summary, the ORR activity of metal macrocycle complexes is governed by the relative position of the d_{z^2} orbital of Fe in comparison to the Fermi level, leading to the peak positions of the unoccupied O2p orbital in comparison to the Fermi level. The optimized adsorption strengths of the ORR intermediates could be achieved by controlling the d_{z^2} orbital level, which could be downshifted by the attachment of electron withdrawing functional groups.

It has been proposed that the main degradation mechanism of Fe–N_4 chelate macrocycle catalysts in acidic electrolytes is the demetalation of the macrocycles.[43,49] This leads to a dramatic loss in the ORR performance because the resulting H_2Pc materials have very limited activity.[53,61] The demetalation process is highlighted in reaction (13):

$$\text{Fe-(S)Pc} + 2\text{H}^+ = \text{H}_2\text{(S)Pc} + \text{Fe}^{+2} \quad (13)$$

The redox couples of Fe-Pc and Fe-SPc observed in the cyclic voltammograms (CV) of Fig. 9a and b indicate the presence of the Fe-ion centers in the macrocycle complexes. Diminishing charges of the redox couple can therefore provide evidence of the Fe–N4 demetalation.[33,60,61] Fig. 9 clearly demonstrates that functionalized diphenyl thiophenol groups on the Fe-Pc dramatically enhance the stability of Fe-SPc over 100 cycles in the oxygen-saturated electrolyte. After 100 cycles, the CV curve of Fe-Pc exhibits a significant loss in the redox charge transfer of Fe in comparison to the initial plot (Fig. 9a). This observation is in agreement with the significant loss of ORR activity (Fig. 9b), indicating the occurrence of Fe-Pc demetalation under these conditions. On the other hand, after 100 cycles, Fe-SPc still maintains the distinct Fe-ion redox peaks (Fig. 9c), and shows only a 20.3 mV loss in the half-wave potential for the ORR (Fig. 9d).

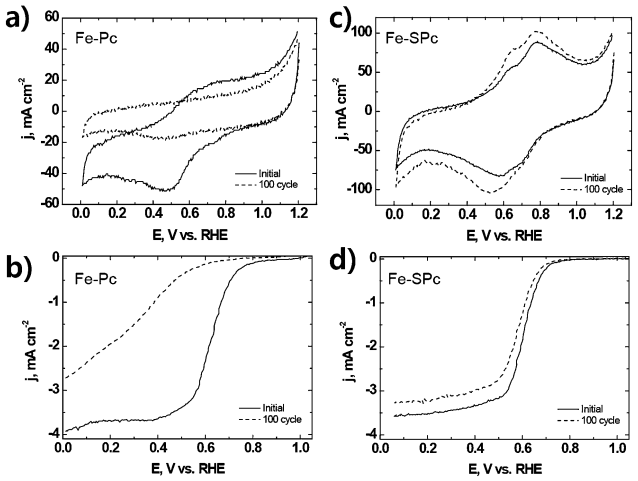

Fig. 9 (a and c) Cyclic voltammograms and (b and d) ORR polarization curves on Fe-Pc/KJ300 and Fe-SPc/KJ300 before and after 100 potential cycles in O_2-saturated 0.1 M $HClO_4$. This data is reproduced from ref. 23, Copyright 2010, with permission of The American Chemical Society.

This pronounced increase in the electrochemical stability of the Fe-SPc macrocycle is of high interest, and has been investigated by calculating the cohesive energies (E_{coh}) of Fe and FeO in the ferrous phthalocyanine macrocycle complexes through the first principle calculations using eqn (14) and (15) as follows:

$$E_{coh} = -(E_{\text{Fe-(S)Pc}} - E_{\text{(S)Pc}} - E_{\text{Fe,g}}) \quad (14)$$

$$E_{coh} = -(E_{\text{FeO-(S)Pc}} - E_{\text{(S)Pc}} - E_{\text{FeO,g}}) \quad (15)$$

here, $E_{\text{FeO-(S)Pc}}$ is the total energy of the O adsorbed onto Fe-Pc and Fe-SPc, $E_{\text{Fe,g}}$ and $E_{\text{FeO,g}}$ are total energy of Fe and FeO in the gas phase, and $E_{\text{(S)Pc}}$ is total energy of the phthalocyanine macrocycle frame of Fe-Pc and Fe-SPc without the central Fe atom. In the case of metals, it has been proposed that the cohesive energy and electrochemical dissolution potential of the metal are strongly correlated,[22,72,75–78] and a higher cohesive energy of the metal indicates a higher dissolution potential. Thus, the cohesive energies of Fe or FeO in the macrocycle complexes are likely to be related to the durability of iron based materials under harsh conditions. DFT predicts, however, that the cohesive energy of Fe in the macrocycle complex is 9.80 eV for Fe-Pc, which is higher than 9.53 eV for Fe-SPc. These results do not align with our electrochemical measurements in acidic electrolytes discussed previously. Therefore, to provide reasonable explanation surrounding the observed demetalation of the ferrous phthalocyanine complex, the presence of oxygen requires further consideration. In fact, it was found that the demetalation and activity losses of Fe-Pc and Fe-SPc were minimized under inert atmospheres, whereas the activity was significantly compromised in the presence of oxygen that would attack the active site structures.[33,53] When oxygen is adsorbed onto Fe-Pc and Fe-SPc, the electron transfer from the central metal to the oxygen molecule could decrease the atomic radius of the central Fe, and thus the distance of the Fe–N bonds could be increased.[33,53] Even in this work, the distance between the central Fe and N atoms is increased from *ca.* 1.93 Å to 1.96 Å for FePc and Fe-SPc upon the adsorption of oxygen, and these results agree well with previous investigations.[53,79] The FeO cohesive energy of 10.22 eV for Fe-SPc is higher than 10.15 eV for Fe-Pc, as summarized in Table 1, thereby indicating that the electrochemical stability in the presence of oxygen for Fe-SPc is enhanced in comparison to Fe-Pc. Therefore, the diphenyl thiophenol electron donating groups substituted onto the phthalocyanine complex could exclusively help to suppress the demetalation and enhance the stability of Fe-SPc in the presence of oxygen, which is the necessary reactant at the cathode of PEMFCs.

4. Conclusion

Using first-principles DFT calculations, we have studied the scientifically relevant ORR processes occurring on Fe-Pc and Fe-SPc materials in terms of electrochemical activity and stability.

The results indicate that the d_{z^2} orbital in the DOS is closely related with ORR activity, showing electronic d_{z^2} orbital splitting into bonding and antibonding states before and after the adsorption of O_2. The position of the d_{z^2} orbital of Fe in comparison to the Fermi level, a factor related to the unoccupied ΔO2p orbital level, ultimately determines the ORR onset potential and oxygen intermediate adsorption strengths of metal macrocycle complexes, owing to the modulated electron transfer capabilities to the O atom. The free energy diagram clearly indicates that a rate determining step is in the reduction step of O* to OH*, which indicates that the overall ORR kinetics are governed by the oxygen adsorption strength on Fe-Pc and Fe-SPc. The relatively upward shift of the d_{z^2} orbital of the Fe atom in Fe-SPc provides stronger bonding of the oxygen intermediates, leading to a reduction in the activity towards the ORR. This prediction is consistent with the results from electrochemical testing carried out in O_2-saturated acidic condition, wherein the on-set potential and a half-wave potential of Fe-SPc/KJ300 was reduced in comparison to Fe-Pc/KJ300. The free energy diagram prepared using DFT also predicts the same activity trends, wherein the activity of Fe-SPc is slightly lower than that of Fe-Pc. It is therefore clear that the optimized adsorption strengths of the ORR intermediates can be achieved by carefully tuning the level of the d_{z^2} orbital. Interestingly, the electrochemical stability of Fe-SPc, evaluated by accelerated testing protocols, was significantly enhanced in the presence of oxygen in comparison to Fe-Pc. This observation can be explained using theoretical calculations, which show an increased cohesive energy of FeO for Fe-SPc in comparison to Fe-Pc. Furthermore, the diphenyl thiophenol electron donating groups substituted onto the phthalocyanine complex could help suppress the demetalation of the macrocycle structure by providing extra electrons to the metal ion center. Since these investigated electronic properties can be directly modulated by the appropriate selection and attachment of various substituent groups on the transition metal macrocycles, this comprehensive DFT study linked to experimental observations can provide the fundamental basis for the design of future generation non-precious ORR catalysts with improved activity and stability.

Acknowledgements

The authors specially thank Mr Hey Woong Park at the University of Waterloo for discussion and comments. Financial support was provided by the DOE-EERE Fuel Cell Technologies Program (Project ID: FC107) for non-precious metal catalysis research led by the Los Alamos National Laboratory and the Catalysis Research for Polymer Electrolyte Fuel Cells (CaRPE FC) Network, which was administered from Simon Fraser University and supported by Automotive Partnership Canada (APC) Grant no. APCPJ 417858-11 through the Natural Sciences and Engineering Research Council of Canada (NSERC). This research was also enabled by the use of computing resources provided by WestGrid and Compute/Calcul Canada and Korea Institute of Science and Technology Information (KISTI, KSC-2013-C2-008 and KSC-2013-C2-054) and by supported from the Global Frontier R&D Program (2013-073298) on Center for Hybrid Interface Materials (HIM), funded by the Ministry of Science, ICT & Future Planning. The New and Renewable Energy R&D Program (2013M3A6B1078882) and the Leading Foreign Research Institute Recruitment Program through the National Research Foundation of Korea (NRF) under the Ministry of Knowledge Economy, Republic of Korea partly supported this research work.

References

1 H. W. Park, D. U. Lee, L. F. Nazar and Z. W. Chen, *J. Electrochem. Soc.*, 2013, **160**, A344–A350.
2 D. U. Lee, H. W. Park, D. Higgins, L. Nazar and Z. W. Chen, *J. Electrochem. Soc.*, 2013, **160**, F910–F915.
3 H. Zhang, X. Zhong, J. C. Shaw, L. X. Liu, Y. Huang and X. F. Duan, *Energy Environ. Sci.*, 2013, **6**, 2621–2625.
4 J. L. Shui, J. S. Okasinski, P. Kenesei, H. A. Dobbs, D. Zhao, J. D. Almer and D. J. Liu, *Nat. Commun.*, 2013, **4**, 2255.
5 D. Higgins, Z. Chen, D. U. Lee and Z. Chen, *J. Mater. Chem. A*, 2013, **1**, 2639–2645.
6 N. Lopez, D. J. Graham, R. McGuire, G. E. Alliger, Y. Shao-Horn, C. C. Cummins and D. G. Nocera, *Science*, 2012, **335**, 450–453.
7 M. W. Kanan and D. G. Nocera, *Science*, 2008, **321**, 1072–1075.
8 W. Vielstich, A. Lamm and H. A. Gasteiger, *Handbook of Fuel Cells Fundamentals Technology and Applications*, John Wiley & Sons Ltd., London, 2003.
9 F. Bidault, D. J. L. Brett, P. H. Middleton and N. P. Brandon, *J. Power Sources*, 2009, **187**, 39–48.
10 J. S. Park, S. H. Park, S. D. Yim, Y. G. Yoon, W. Y. Lee and C. S. Kim, *J. Power Sources*, 2008, **178**, 620–626.
11 K. Asazawa, K. Yamada, H. Tanaka, A. Oka, M. Taniguchi and T. Kobayashi, *Angew. Chem.*, 2007, **119**, 8170–8173.
12 K. A. Kuttiyiel, K. Sasaki, Y. Choi, D. Su, P. Liu and R. R. Adzic, *Energy Environ. Sci.*, 2012, **5**, 5297.
13 H. Xu, Q. Fu, Y. Yao and X. Bao, *Energy Environ. Sci.*, 2012, **5**, 6313.
14 M. Oezaslan, F. Hasche and P. Strasser, *J. Electrochem. Soc.*, 2012, **159**, B444–B454.
15 M. Winter and R. J. Brodd, *Chem. Rev.*, 2004, **104**, 4245–4269.
16 W. Vielstich, A. Lamm and H. A. Gasteiger, *Handbook of fuel cells fundamentals technology and applications*, John Wiley & Sons Ltd., London, 2003.
17 N. N. Kariuki, W. J. Khudhayer, T. Karabacak and D. J. Myers, *ACS Catal.*, 2013, **3**, 3123–3132.
18 L. Tang, B. Han, K. Persson, C. Friesen, T. He, K. Sieradzki and G. Ceder, *J. Am. Chem. Soc.*, 2009, **132**, 596–600.
19 Y. Shao-Horn, W. C. Sheng, S. Chen, P. J. Ferreira, E. F. Holby and D. Morgan, *Top. Catal.*, 2007, **46**, 285–305.
20 Y. Shao, G. Yin and Y. Gao, *J. Power Sources*, 2007, **171**, 558–566.
21 D. Higgins, M. A. Hoque, M. H. Seo, R. Wang, F. Hassan, J.-Y. Choi, M. Pritzker, A. Yu, J. Zhang and Z. Chen, *Adv. Funct. Mater.*, 2014, **24**, 4325–4336.

22 M. H. Seo, S. M. Choi, E. J. Lim, I. H. Kwon, J. K. Seo, S. H. Noh, W. B. Kim and B. Han, *ChemSusChem*, 2014, **7**, 2609–2620.
23 R. Bashyam and P. Zelenay, *Nature*, 2006, **443**, 63–66.
24 L. Qu, Y. Liu, J.-B. Baek and L. Dai, *ACS Nano*, 2010, **4**, 1321–1326.
25 D. Deng, X. Pan, L. Yu, Y. Cui, Y. Jiang, J. Qi, W.-X. Li, Q. Fu, X. Ma, Q. Xue, G. Sun and X. Bao, *Chem. Mater.*, 2011, **23**, 1188–1193.
26 Z. Chen, D. Higgins, A. Yu, L. Zhang and J. Zhang, *Energy Environ. Sci.*, 2011, **4**, 3167.
27 H. Chung, C. Johnson, K. Artyushkova, M. Ferrandon, D. Myers and P. Zelenay, *Electrochem. Commun.*, 2010, **12**, 1792–1795.
28 E. Proietti, F. Jaouen, M. Lefevre, N. Larouche, J. Tian, J. Herranz and J. P. Dodelet, *Nat. Commun.*, 2011, **2**, 416.
29 W. M. Li, J. Wu, D. C. Higgins, J. Y. Choi and Z. W. Chen, *ACS Catal.*, 2012, **2**, 2761–2768.
30 F. Jaouen, E. Proietti, M. Lefevre, R. Chenitz, J.-P. Dodelet, G. Wu, H. T. Chung, C. M. Johnston and P. Zelenay, *Energy Environ. Sci.*, 2011, **4**, 114.
31 G. Wu, K. L. More, C. M. Johnston and P. Zelenay, *Science*, 2011, **332**, 443–447.
32 M. Lefevre, E. Proietti, F. Jaouen and J. P. Dodelet, *Science*, 2009, **324**, 71–74.
33 W. Li, A. Yu, D. C. Higgins, B. G. Llanos and Z. Chen, *J. Am. Chem. Soc.*, 2010, **132**, 17056–17058.
34 N. Ramaswamy, U. Tylus, Q. Jia and S. Mukerjee, *J. Am. Chem. Soc.*, 2013, **135**, 15443–15449.
35 Y. Bing, H. Liu, L. Zhang, D. Ghosh and J. Zhang, *Chem. Soc. Rev.*, 2010, **39**, 2184–2202.
36 R. R. Adzic, J. Zhang, K. Sasaki, M. B. Vukmirovic, M. Shao, J. Wang, A. U. Nilekar, M. Mavrikakis, J. Valerio and F. Uribe, *Top. Catal.*, 2007, **46**, 249–262.
37 P. Mani, R. Srivastava and P. Strasser, *J. Power Sources*, 2011, **196**, 666–673.
38 B. Hammer and J. K. Norskov, *Nature*, 1995, **376**, 238–240.
39 J. Greeley, I. E. L. Stephens, A. S. Bondarenko, T. P. Johansson, H. A. Hansen, T. F. Jaramillo, J. Rossmeisl, I. Chorkendorff and J. K. Nørskov, *Nat. Chem.*, 2009, **1**, 552–556.
40 M. Shao, K. Sasaki, N. S. Marinkovic, L. Zhang and R. R. Adzic, *Electrochem. Commun.*, 2007, **9**, 2848–2853.
41 M. H. Shao, P. Liu, J. Zhang and R. R. Adzic, *J. Phys. Chem. B*, 2007, **111**, 6772–6775.
42 H. M. P. K. Shen, *Electrochem. Commun.*, 2006, **8**, 588–594.
43 M.-S. Liao and S. Scheinera, *J. Chem. Phys.*, 2002, **117**, 205.
44 P. Hohenberg and W. Kohn, *Phys. Rev.*, 1964, **136**, B864–B871.
45 W. Kohn and L. J. Sham, *Phys. Rev.*, 1965, **140**, A1133–A1138.
46 G. Kresse and J. Furthmüller, *Phys. Rev. B: Condens. Matter Mater. Phys.*, 1996, **54**, 11169.
47 J. P. Perdew, K. Burke and M. Ernzerhof, *Phys. Rev. Lett.*, 1996, **77**, 3865.
48 G. Kresse and J. Furthmuller, *Comput. Mater. Sci.*, 1996, **6**, 15.
49 G. Kresse and D. Joubert, *Phys. Rev. B: Condens. Matter Mater. Phys.*, 1999, **59**, 1758.
50 P. E. Blöchl, *Phys. Rev. B: Condens. Matter Mater. Phys.*, 1994, **50**, 17953.
51 M. Methfessel and A. T. Paxton, *Phys. Rev. B: Condens. Matter Mater. Phys.*, 1989, **40**, 3616–3621.
52 K. M. Ho, C. L. Fu, B. N. Harmon, W. Weber and D. R. Hamann, *Phys. Rev. Lett.*, 1982, **49**, 673–676.
53 S. Baranton, C. Coutanceau, C. Roux, F. Hahn and J. M. Leger, *J. Electroanal. Chem.*, 2005, **577**, 223–234.
54 D. R. Lide, *CRC handbook of chemistry and physics*, 86th edn, 2005.
55 B. I. Lundqvist, O. Gunnarsson, H. Hjelmberg and J. K. Norskov, *Surf. Sci.*, 1979, **89**, 196–225.
56 B. Hammer and J. K. Nørskov, *Adv. Catal.*, 2000, **45**, 71–129.
57 J. E. Huheey, E. A. Keiter and R. L. Keiter, *Inorganic Chemistry: Principles of Structure and Reactivity*, Prentice Hall, 1997.
58 H. Nakashima, J. Y. Hasegawa and H. Nakatsuji, *J. Comput. Chem.*, 2006, **27**, 426–433.
59 A. R. Albuquerque, J. Maul, E. Longo, I. M. G. d. Santos and A. J. R. Sambrano, *J. Phys. Chem. C*, 2013, **117**, 7050–7061.
60 J. Zagal, P. Bindra and E. Yeager, *J. Electrochem. Soc.*, 1980, **127**, 1506–1517.
61 J. Zagal, M. Paez, A. A. Tanaka, J. R. Dossantos and C. A. Linkous, *J. Electroanal. Chem.*, 1992, **339**, 13–30.
62 N. Ramaswamy and S. Mukerjee, *Adv. Phys. Chem.*, 2012, **2012**, 17.
63 M. H. Seo, S. M. Choi, H. J. Kim and W. B. Kim, *Electrochem. Commun.*, 2011, **13**, 182–185.
64 J. Guo, A. Hsu, D. Chu and R. Chen, *J. Phys. Chem. C*, 2010, **114**, 4324–4330.
65 N. M. Markovic, B. N. Grgur and P. N. Ross, *J. Phys. Chem. B*, 1997, **101**, 5405–5413.
66 U. A. Paulus, T. J. Schmidt, H. A. Gasteiger and R. J. Behm, *J. Electroanal. Chem.*, 2001, **495**, 134–145.
67 K. J. J. Mayrhofer, D. Strmcnik, B. B. Blizanac, V. Stamenkovic, M. Arenz and N. M. Markovic, *Electrochim. Acta*, 2008, **53**, 3181–3188.
68 H. Kim, K. Lee, S. I. Woo and Y. Jung, *Phys. Chem. Chem. Phys.*, 2011, **13**, 17505–17510.
69 H. Tominaga, W. Ikeda and M. Nagai, *Phys. Chem. Chem. Phys.*, 2011, **13**, 2659–2662.
70 J. K. Nørskov, J. Rossmeisl, A. Logadottir, L. Lindqvist, J. R. Kitchin, T. Bligaard and H. Jónsson, *J. Phys. Chem. B*, 2004, **108**, 17886–17892.
71 S. F. Huang, K. Terakura, T. Ozaki, T. Ikeda, M. Boero, M. Oshima, J. Ozaki and S. Miyata, *Phys. Rev. B*, 2009, **80**, 235410.
72 B. Han, V. Viswanathan and H. Pitsch, *J. Phys. Chem. C*, 2012, **116**, 6174–6183.
73 S. H. Noh, D. H. Kwak, M. H. Seo, T. Ohsaka and B. Han, *Electrochim. Acta*, 2014, **140**, 225–231.
74 P. Atkins and J. D. Paula, *Physical Chemistry*, Oxford University Press, Oxford, UK, 8th edn, 2006.
75 J. K. Seo, A. Khetan, M. H. Seo, H. Kim and B. Han, *J. Power Sources*, 2013, **238**, 137–143.

76 S. H. Noh, M. H. Seo, J. K. Seo, P. Fischer and B. Han, *Nanoscale*, 2013, **5**, 8625–8633.
77 L. Tang, B. Han, K. Persson, C. Friesen, T. He, K. Sieradzki and G. Ceder, *J. Am. Chem. Soc.*, 2010, **132**, 596–600.
78 W. H. Qi and M. P. Wang, *J. Mater. Sci. Lett.*, 2002, **21**, 1743–1745.
79 I. C. Stefan, Y. B. Mo, S. Y. Ha, S. Kim and D. A. Scherson, *Inorg. Chem.*, 2003, **42**, 4316–4321.